Bioactive Materials 51 (2025) 293–305

Contents lists available at ScienceDirect

Bioactive Materials

journal homepage: www.keaipublishing.com/en/journals/bioactive-materials

Tryptophan-producing bacteria to mitigate osteoporosis and intestinal dysfunction

Bo Tian [a,1], Heng Wang [b,1], Yue Zhang [b,1], Jinmin Lv [a], Dongxiao Li [b], Chenmeng Zhou [b], Jialu Xu [b], Yichao Ni [a], Bingbing Wu [b], Mingchao Zhang [a], Huaxing Dai [b], Fang Xu [b], Jinyu Bai [a,*], Chao Wang [b,**], Xiaozhong Zhou [a,***]

[a] Department of Orthopedics, The Second Affiliated Hospital of Soochow University, Suzhou, Jiangsu, 215004, China
[b] Laboratory for Biomaterial and Immunoengineering, Institute of Functional Nano & Soft Materials (FUNSOM), Jiangsu Key Laboratory for Carbon-based Functional Materials and Devices, Soochow University, Suzhou, Jiangsu, 215123, China

A B S T R A C T

The relationship between gut microbiota and host health and disease is intricate, with microbiota-derived metabolites playing a crucial role in the gut-organ axis. In this study, we observe significantly decreased levels of microbial metabolites, particularly tryptophan derivatives in osteoporosis mice. Loss of tryptophan induced intestinal epithelial barrier dysfunction which compromised intestinal barrier integrity, leading to bone inflammatory responses and pathological osteoporosis. Through supplementation of tryptophan-producing bacteria, we effectively repair damaged intestinal barriers in colitis mice and mitigate bone loss, indicating the link between chronic colitis and osteoporosis. This approach offers a promising synthetic biology-based strategy to improve osteoporosis therapy by targeting gut tryptophan. This intervention also alleviates age-related osteoporosis in an aged mouse model, providing a potential therapeutic avenue for combating osteoporosis, a disease of growing concern in aging populations.

1. Introduction

The prevailing understanding of organismal physiology underscores the interconnectedness of various organs, highlighting their collaborative rather than isolated functions. The gastrointestinal tract, beyond its fundamental role as a digestive organ, emerges as the body's largest immune organ, engaging in intricate crosstalk with multiple organ systems [1–4]. As investigations into the relationship between gut microbiota and host disease have gained traction [5], the exploration of various axes including the gut-brain, gut-liver, gut-lung, gut-heart, gut-skin, and gut-adipose axes has flourished in recent years [6–12].

Despite the wealth of research in this area, the gut-bone axis remains relatively underexplored. Several studies have indicated a notable alteration in the gut microbiome composition of individuals suffering from osteoporosis, suggesting a hidden link between intestinal health and bone density [13–18]. Experimental studies have revealed that mice raised in germ-free conditions displayed an increase in bone mass compared to those bred under conventional conditions. Normalization of bone mass was observed following colonization with a normal gut microbiome, underscoring the potential significance of gut homeostasis in skeletal health [19]. However, the underlying mechanism of how the gut influences bone mass is not very clear, which warrants further exploration. In addition, it also opens up possibilities that pathological situations in the gut, such as chronic infection, colitis and aging that are characterized by gut inflammatory responses can affect bone immunity, leading to bone-related diseases. Chronic colitis is often associated with a dysregulated immune response in the gut, leading to persistent inflammation and damage to the intestinal barrier [20]. Aging further complicates this relationship, as the aging process is characterized by a decline in gut barrier integrity and an increase in systemic inflammation [21].

In this study, we observe that chronic colitis can lead to osteoporosis in mice models. We further reveal that chronic colitis leads to a "leaky gut", which induces osteoporosis by disputing the bone immune microenvironment. We elucidate the regulatory role of microbial metabolites in modulating intestinal epithelial barrier function, showing

Peer review under the responsibility of editorial board of Bioactive Materials.
* Corresponding author.
** Corresponding author.
*** Corresponding author.
E-mail addresses: baijy@suda.edu.cn (J. Bai), cwang@suda.edu.cn (C. Wang), zhouxz@suda.edu.cn (X. Zhou).
[1] Equally contribution.

https://doi.org/10.1016/j.bioactmat.2025.05.013
Received 25 February 2025; Received in revised form 25 April 2025; Accepted 13 May 2025

tryptophan metabolism is significantly altered in chronic colitis mice. Recent studies show that tryptophan and its microbial metabolites assume crucial roles in maintaining intestinal barrier function [22–24]. Tryptophan acts through receptors such as the aryl hydrocarbon receptor [24–27] and dopamine receptors [22] in maintaining intestinal barrier integrity. We then engineer a tryptophan-producing probiotic to treat these colitis mice. Interestingly, the integrity of the gut barrier is rescued, and more importantly, the osteoporosis is alleviated in these colitis mice. Our results indicate the integrity of the gut barrier is important to maintain the bone mass. Furthermore, in a senile mouse model with low-level chronic information within the gut, tryptophan demonstrates significant improvements in bone mass, indicating a novel therapy strategy for osteoporosis treatment in aging populations. Leveraging insights from the gut-bone axis, the tailored design and synthesis of engineered probiotics offer a convenient and effective therapeutic strategy for osteoporosis in aging populations.

2. Results

2.1. Impact of colitis on bone metabolism

To investigate the effect of intestinal inflammation on skeletal health, we established models of colitis in mice (Supplementary Fig. 1A and 1A–D) according to previous studies [28–30]. We investigated the

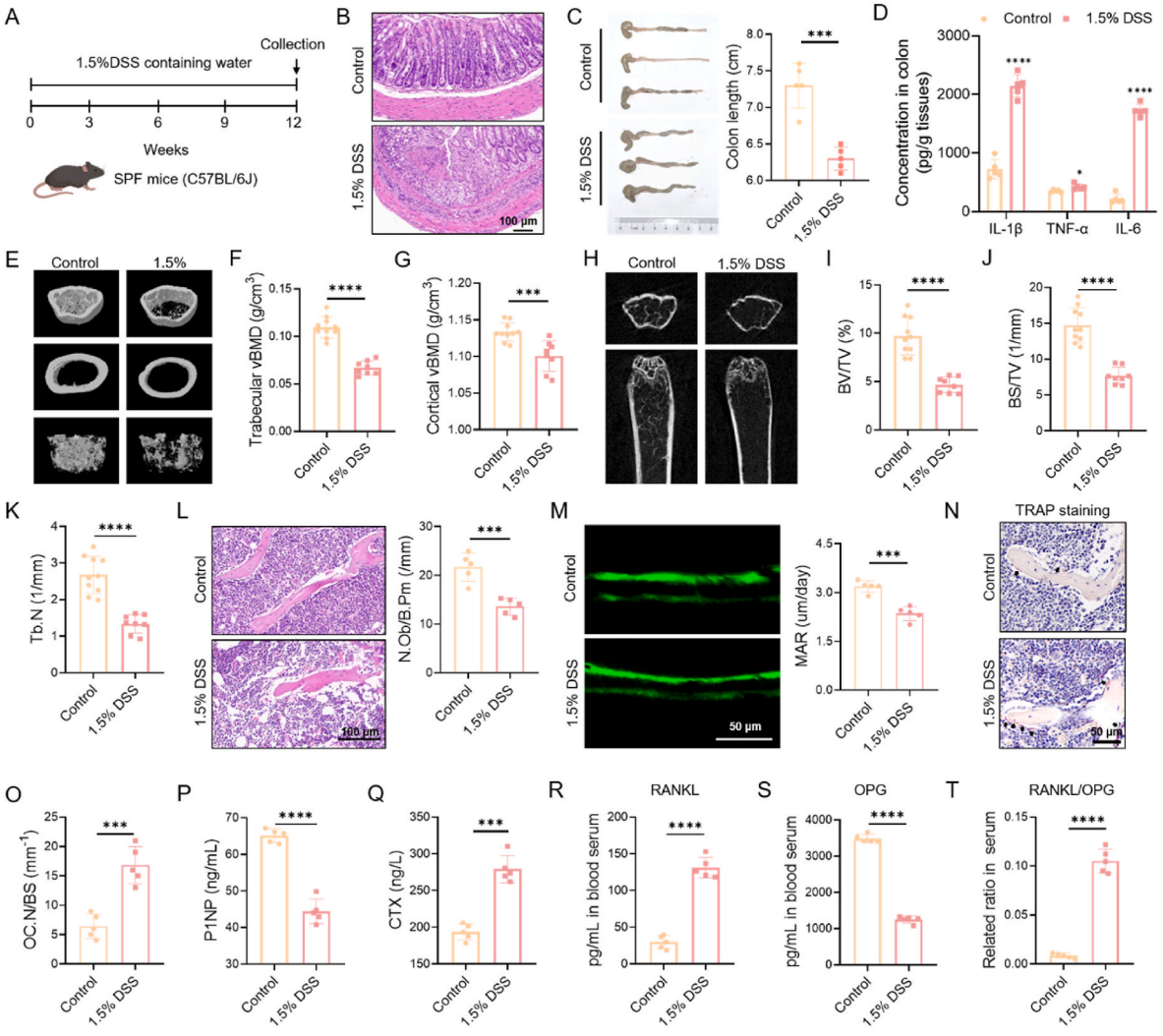

Fig. 1. Impact of Chronic Colitis on Bone Metabolism. A. Schematic illustration of the chronic colitis model establishment. **B.** Representative Hematoxylin and Eosin (H&E) stained sections of intestinal tissue. Scale bar: 100 μm. **C.** Gross morphology and quantitative analysis of colon length across different experimental groups. **D.** Levels of inflammatory cytokines in intestinal tissues, quantified to demonstrate elevated inflammation in the colitis model. **E.** Micro-computed tomography (μCT) three-dimensional reconstructions of mouse femurs, illustrating structural changes in the bone due to colitis. **F.** Quantitative analysis of trabecular bone density derived from μCT data (Control: n = 10; 1.5 %DSS: n = 8). **G.** Quantitative analysis of cortical bone density, also derived from μCT data (Control: n = 10; 1.5 %DSS: n = 8). **H.** Representative μCT images of mouse femurs, providing insight into bone microarchitecture. **I.** Measurement of Bone Volume to Total Volume Ratio (BV/TV) (Control: n = 10; 1.5 %DSS: n = 8). **J.** Measurement of Bone Surface to Total Volume Ratio (BS/TV) (Control: n = 10; 1.5 %DSS: n = 8). **K.** Measurement of Trabecular Number (Tb.N), evaluating trabecular structures within the bone (Control: n = 10; 1.5 %DSS: n = 8). **L.** Representative H&E stained sections of femoral bone tissue with quantitative analysis. Scale bar: 100 μm. **M.** Calcein labeling to visualize bone formation, with quantification of Mineral Apposition Rate (MAR). Scale bar: 50 μm. **N** and **O.** Representative Tartrate-resistant Acid Phosphatase (TRAP) staining of femoral bone sections, quantifying osteoclast activity. Scale bar: 50 μm. **P.** Serum levels of Procollagen Type 1 N-Terminal Propeptide (P1NP), a biomarker of osteoblast activity. **Q.** Serum levels of C-terminal Telopeptide of Type I Collagen (CTX), indicative of osteoclast-mediated bone resorption. **R.** Serum levels of Receptor Activator of Nuclear Factor Kappa-B Ligand (RANKL), crucial for osteoclast differentiation and activation. **S.** Serum levels of Osteoprotegerin (OPG), a decoy receptor that inhibits RANKL. **T.** Ratio of RANKL to OPG, providing insight into the regulatory balance of bone remodeling. Data are presented as mean ± SD; statistical significance was calculated by the Student's t-tests. $*p < 0.05$, $**p < 0.01$, $***p < 0.001$, and $****p < 0.0001$. n = 5.

bone architecture in chronic colitis mice using three-dimensional micro-computerized tomography (μCT). Compared to the controls, mice with induced colitis exhibited significant reductions in bone mass and alterations in bone parameters. Although the acute colitis model (7 days) was shorter than the conventional 8-week OVX osteoporosis model [31], colitis induced high levels of systemic inflammation, which led to observable trabecular bone loss. Compared to the control group, acute colitis mice showed reductions in trabecular bone density, trabecular bone volume, bone surface area, and trabecular number, along with a significant increase in total porosity (Supplementary Fig. 1B–H). After 12 weeks of chronic colitis modeling, bone loss in the femur was more severe, with significant reductions in both trabecular and cortical bone density and marked trabecular loss in 2D CT images. Trabecular bone volume, bone surface area, and trabecular number were more significantly reduced in the chronic colitis group (Fig. 1E–K). Further confirmation of μCT findings was sought through detailed histological examinations of the femoral bones. Hematoxylin and Eosin (H&E) staining revealed a pronounced decrease in trabecular bone structure in the colitis models (Fig. 1L). Calcein labeling, used to assess bone formation, showed reduced activity in these mice (Fig. 1M), indicating a compromised bone-forming capacity. Additionally, Tartrate-resistant acid phosphatase (TRAP) staining highlighted an increase in osteoclast numbers (Fig. 1N–O), signifying enhanced bone resorption. The serological analysis further supported these histological findings, revealing significant changes in markers of bone metabolism including Procollagen Type 1 N-Terminal Propeptide (P1NP) and

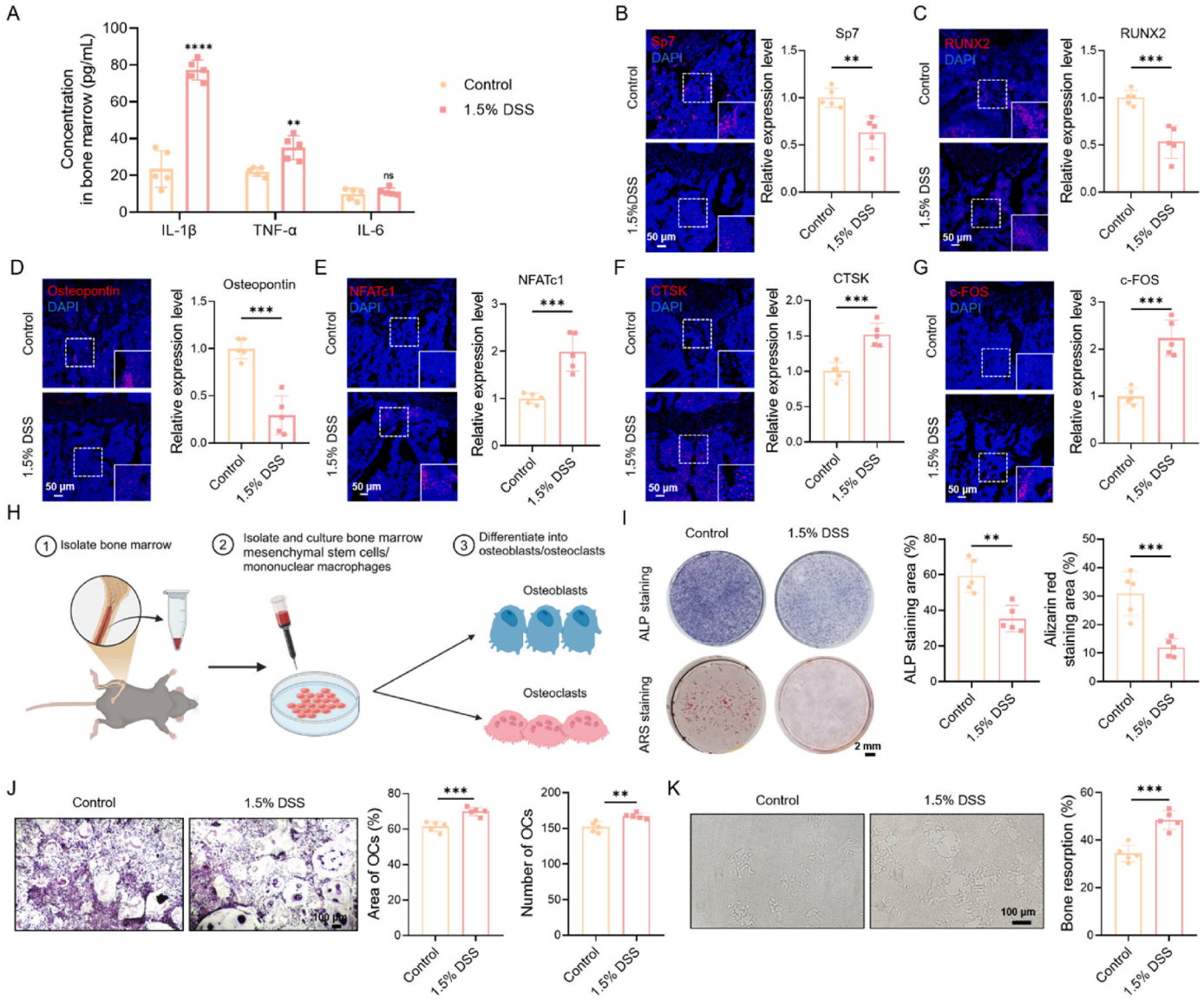

Fig. 2. Effect of Inflammatory Mediators on Bone Remodeling. **A.** Levels of inflammatory cytokines in bone marrow across different experimental groups, illustrating the inflammatory milieu in the bone environment. Immunofluorescence imaging demonstrated the expression of osteoblast-specific proteins Sp7 (**B**), RUNX2 (**C**), and Osteopontin (**D**) in bone tissues. Scale bar: 50 μm. Immunofluorescence imaging demonstrated the expression of osteoclast-specific proteins NFATc1 (**E**), CTSK (**F**), and c-FOS (**G**) in bone tissues. Scale bar: 50 μm. **H.** Schematic representation of *in vitro* experiments involving osteogenic induction of bone marrow-derived mesenchymal stem cells (MSCs) and osteoclastogenic induction of bone marrow-derived mononuclear macrophages. **I.** Representative images and quantitative analysis of Alkaline Phosphatase (ALP) and Alizarin Red S (ARS) staining showing osteogenic differentiation and mineralization of bone marrow-derived MSCs. Scale bar: 2 mm. **J.** Representative images and quantitative analysis of TRAP staining for osteoclast differentiation in bone marrow-derived mononuclear macrophages. Scale bar: 100 μm. **K.** Bone resorption assay demonstrating pit formation and quantitative analysis of bone resorption activity in osteoclasts derived from bone marrow. Scale bar: 100 μm. Data are presented as mean ± SD; statistical significance was calculated by the Student's t-tests. *$p < 0.05$, **$p < 0.01$, ***$p < 0.001$, and ****$p < 0.0001$. n = 5.

C-terminal Telopeptide of Type I Collagen (CTX) (Fig. 1P–Q). Additionally, alterations in the regulatory pathway involved in osteoclastogenesis were evident. Serum levels of Receptor Activator of Nuclear Factor Kappa-B Ligand (RANKL) were upregulated, whereas Osteoprotegerin (OPG) was downregulated, leading to a significant increase in the RANKL/OPG ratio (Fig. 1R–T). This alteration in the RANKL/OPG balance was indicative of an environment conducive to bone loss. All these results indicated that chronic colitis could lead to osteoporosis in mice models, suggesting a detrimental effect of gut inflammation on bone integrity.

2.2. Inflammatory mediators impair bone remodeling

To further characterize the bone immune microenvironment, we detected inflammatory cytokines in the bone marrow. The upregulation of IL-1β and TNF-α in the bone marrow was observed compared to controls, indicating an inflammatory environment conducive to bone remodeling disruption (Fig. 2A). To further evaluate the immune microenvironment of the bone marrow, tissue flow cytometry analysis revealed the activation of multiple immune cell populations (Supplementary Figure 2A). Recent studies have confirmed the impact of increased pro-inflammatory factors in the bone marrow on bone remodeling [32,33]. These inflammatory factors inhibit osteoblast differentiation from bone marrow-derived mesenchymal stem cells (BMSCs) by interfering with Wnt/β-catenin signaling and activate the NF-κB pathway to promote osteoclast differentiation. The IL-1 pathway plays an essential role in the overactivation of osteoclasts, which has been associated with an increased risk of osteoporosis. Changes in these pathways and the transcription of downstream osteogenic and osteoclast-specific genes were further validated (Supplementary Fig. 2B–E). Bone is a dynamic tissue undergoing constant remodeling, with a delicate balance maintained between osteoblast-led bone formation and osteoclast-led bone resorption. Histological analyses further elucidated the impact of bone inflammatory environment on cell function. Fluorescent staining of bone tissue sections revealed a marked decrease in the expression of osteoblast-specific proteins such as osterix (Sp7), RUNX2, and osteopontin, which are critical for bone formation (Fig. 2B–D). Conversely, the expression levels of osteoclast-specific proteins such as nuclear factor of activated T-cells c1 (NFATc1), cathepsin K (CTSK), and c-FOS, which are involved in bone resorption, were significantly elevated (Fig. 2E–G). These findings underscored the shift towards bone resorption in the inflammatory setting.

To further validate these *in vivo* findings, *in vitro* experiments were conducted using bone marrow-derived mesenchymal stem cells from colitis mice (Fig. 2H). Alkaline phosphatase (ALP) activity and Alizarin Red S (ARS) staining, which assess osteogenic differentiation and mineralization, respectively, showed a reduced capacity in BMSCs from colitis model mice (Fig. 2I). This indicated a diminished ability of these cells to differentiate into osteoblasts and form bone under inflammatory conditions. Additionally, TRAP staining and bone pit resorption assays were performed to evaluate the osteoclastogenic potential of bone marrow-derived macrophages from the colitis mice. These experiments revealed an enhanced differentiation into osteoclasts and an increased bone resorption capacity (Fig. 2J–K). This potentiation of osteoclast activity highlighted the direct impact of chronic colitis on bone resorption. Together, these results depicted a scenario where inflammatory mediators from chronic colitis mice significantly impaired bone remodeling by inhibiting osteoblast function and enhancing osteoclast activity.

2.3. Regulation of intestinal epithelial barrier function by tryptophan metabolic pathways

The gut microbiota and its metabolic byproducts play pivotal roles in the homeostasis of the gut. To further explore how chronic colitis influences bone mass *in vivo*, we studied the alteration of gut microbiota and their metabolic byproducts in chronic colitis mice. 16S rRNA sequencing of fecal samples was performed, which revealed significant changes in the microbial community profiles. Notably, the ratio of *Firmicutes* to *Bacteroidetes* increased significantly (Fig. 3A–C), while overall microbial diversity decreased (Supplementary Figure 2F, Fig. 3D–E), indicating a shift in dominant microbial populations (Supplementary Fig. 2G–H). In addition, a segregated metabolite profile was also observed between groups, showing a marked reduction in the levels of short-chain fatty acids (SCFAs), particularly butyrate (Fig. 3F). Untargeted metabolomics involved linear combination of all identified metabolites into new composite variables for principal component analysis (PCA). As shown in Fig. 3G, samples from each group cluster together, and clear separation between groups was observed, indicating good intra-group consistency and significant differences between groups. Interestingly, metabolic set enrichment analysis identified tryptophan pathways were dramatically reduced in chronic colitis mice, while products related to tryptophan metabolism (Kynuuric acid and indole derivatives) were notably downregulated (Fig. 3H–K), suggesting that tryptophan levels in the gut were scarce in chronic colitis mice.

Recent studies showed that tryptophan and its microbial metabolites assume crucial roles in maintaining intestinal barrier function [22–24]. Tryptophan acted through receptors such as the aryl hydrocarbon receptor [24–27] and dopamine receptors [22] in maintaining intestinal barrier integrity. We next investigated the integrity of the gut in chronic colitis mice. As expected, we observed a significant reduction in the expression of the tight junction proteins ZO-1 and occludin (Fig. 3L–M), indicating compromised barrier integrity. Changes in the transcriptional and protein expression levels of ZO-1 and occludin were further validated (Supplementary Fig. 2I–J). The leakage of the gut barrier can trigger inflammation and immune responses throughout the body, contributing to various diseases and conditions. Furthermore, increases in myeloperoxidase (MPO) activity and apoptosis in intestinal epithelial cells were noted (Supplementary Fig. 2K–L), correlating with heightened immune cell activation within the gut (Supplementary Fig. 2M–N).

To further corroborate the crucial role of tryptophan and its microbial metabolites in intestinal barrier function in chronic colitis mice, we genetically engineered a bacterial strain of *Clostridium butyricum* (CB) to produce tryptophan, which could continuously produce tryptophan *in vivo* and demonstrate good biosafety (Supplementary Fig. 3A–D). *Clostridium butyricum* is one of the most common bacteria found in the human gut. We amplified the genes encoding enzymes involved in tryptophan synthesis through an overexpression vector to obtain a high-abundance tryptophan CB strain (Fig. 3N–O and Supplementary Fig. 4A–D). 16S rRNA gene sequencing demonstrated that oral administration of tryptophan-producing probiotics significantly increased microbial community structure diversity, accompanied by a reduction in the *Firmicutes/Bacteroidetes* ratio, suggesting facilitation of gut microbiota homeostasis and restoration of the intestinal epithelial barrier (Supplementary Fig. 4E–M). The levels of SCFAs, especially butyrate, were increased (Supplementary Figure 4N). Non-targeted metabolomics of fecal samples indicated a marked improvement in amino acid metabolism, particularly metabolites related to tryptophan in mice receiving tryptophan-producing probiotics orally (Supplementary Fig. 4O–S). Additionally, tryptophan-producing probiotics treatment led to a restoration of intestinal length in colitis mice (Supplementary Figure 5A) and improvements in tissue architecture, as evidenced by H&E staining (Supplementary Figure 5B). Importantly, we observed that the expression of the tight junction proteins occludin and ZO-1 was remarkably recovered (Fig. 3P–Q), while MPO activity and apoptosis in intestinal epithelial cells were reduced (Supplementary Fig. 5C–D). Changes in the transcriptional and protein expression levels of ZO-1 and occludin were further validated following treatment (Supplementary Fig. 5E–F). The amelioration of intestinal barrier dysfunction subsequently inhibited immune cell activation and reduced inflammatory responses (Supplementary Fig. 5G–I). These results indicated inflammation within the gut, a common pathological feature in conditions like

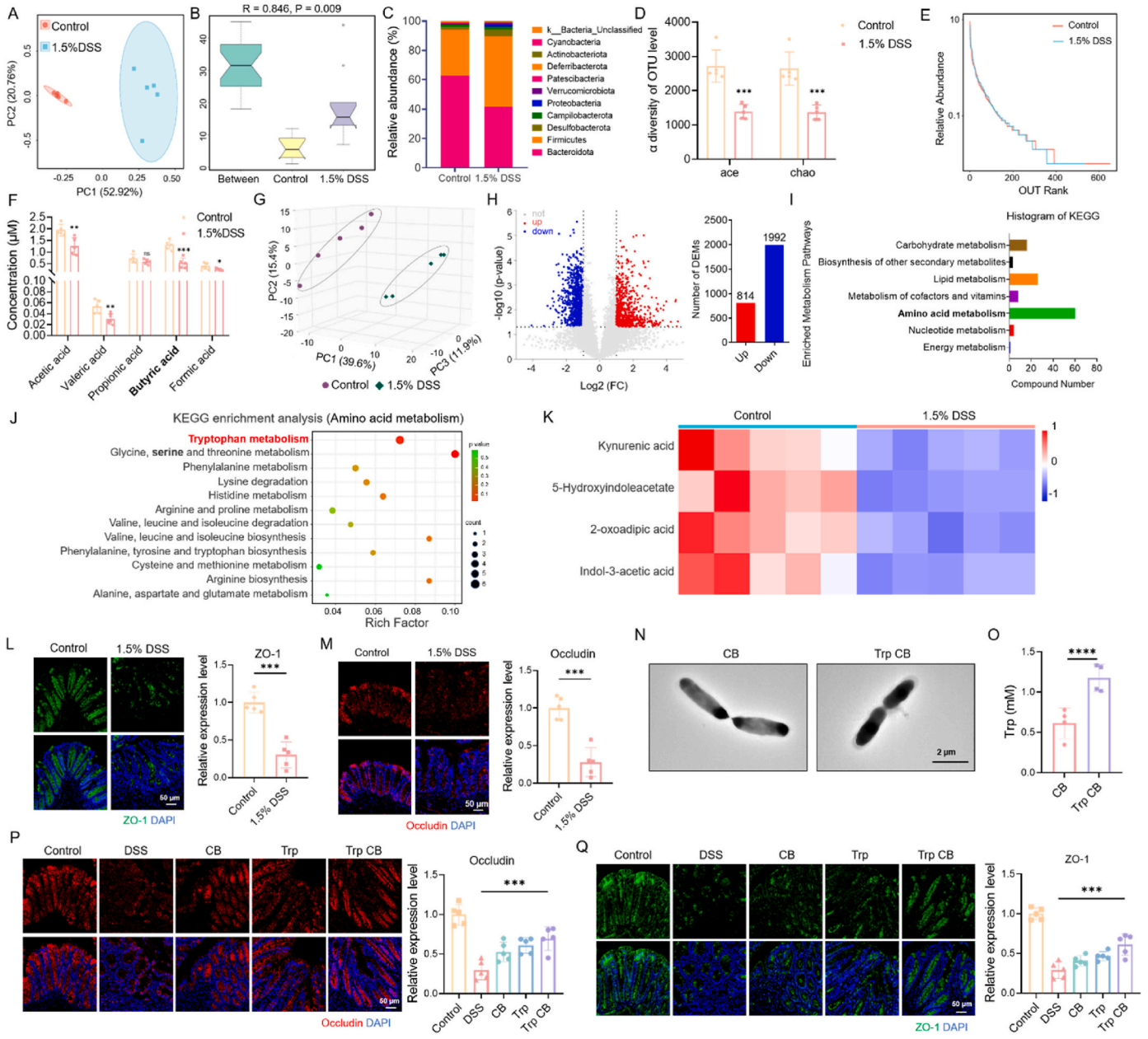

Fig. 3. Effect of Microbial Dysbiosis and Metabolites on Intestinal Barrier Integrity. A. Principal component analysis (PCA) of intestinal microbiota across various groups, illustrating microbial community variation. **B.** Analysis of similarity (Anosim) among groups, demonstrating significant differences in microbial communities. **C.** Relative abundance of microbial species at the phylum level in different groups. **D.** Alpha diversity analysis of intestinal microbiota, assessing species richness within each group. **E.** Rank-abundance curves for microbial diversity analysis, comparing the evenness and richness of microbial species across groups. **F.** Comparative analysis of short-chain fatty acids (SCFAs) in fecal samples from two groups. **G.** Principal component analysis (PCA) of non-targeted metabolomics data, comparing metabolic profiles between groups. **H.** Volcano plot of metabolic changes with quantification of upregulated and downregulated metabolites. **I.** Kyoto Encyclopedia of Genes and Genomes (KEGG) pathway analysis of differential metabolites, identifying impacted metabolic pathways. **J.** KEGG enrichment analysis for amino acid metabolism, elucidating specific pathways under different treatments. **K.** Heatmap of tryptophan metabolism-related products across different groups. **L** and **M.** Representative image showing the expression of the tight junction proteins ZO-1 and occludin in intestinal tissues from different groups. Scale bar: 50 μm. **N.** Morphological comparison of *Clostridium butyricum* (CB) and engineered *Clostridium butyricum* efficiently secreting tryptophan. Scale bar: 2 μm. **O.** Quantitative analysis of tryptophan production by CB and tryptophan-producing probiotic (n = 4). **P** and **Q.** Representative images showing the expression of tight junction proteins occludin and ZO-1 in intestinal tissues of different groups. Scale bar: 50 μm. Data are presented as mean ± SD; statistical significance was calculated by the Student's t-tests or one-way ANOVA. $^{*}p < 0.05$, $^{**}p < 0.01$, $^{***}p < 0.001$, and $^{****}p < 0.0001$. n = 5.

inflammatory bowel disease (IBD) and aging, could disrupt the gut epithelial barrier by disrupting tryptophan metabolic pathways.

2.4. *Tryptophan-producing probiotic alleviated osteoporosis in colitis mice*

We next questioned whether tryptophan-producing probiotics could treat osteoporosis in colitis mice, we orally administered tryptophan-producing probiotics to colitis mice and analyzed the bone mass two weeks later. There was a significant reduction in inflammatory markers in the bone marrow in mice receiving tryptophan-producing probiotics versus untreated colitis mice, indicating the bone inflammation significantly declined (Fig. 4A). To better understand the impact of engineered bacteria on the bone marrow inflammatory microenvironment, flow cytometry showed that the activation of various immune cells was

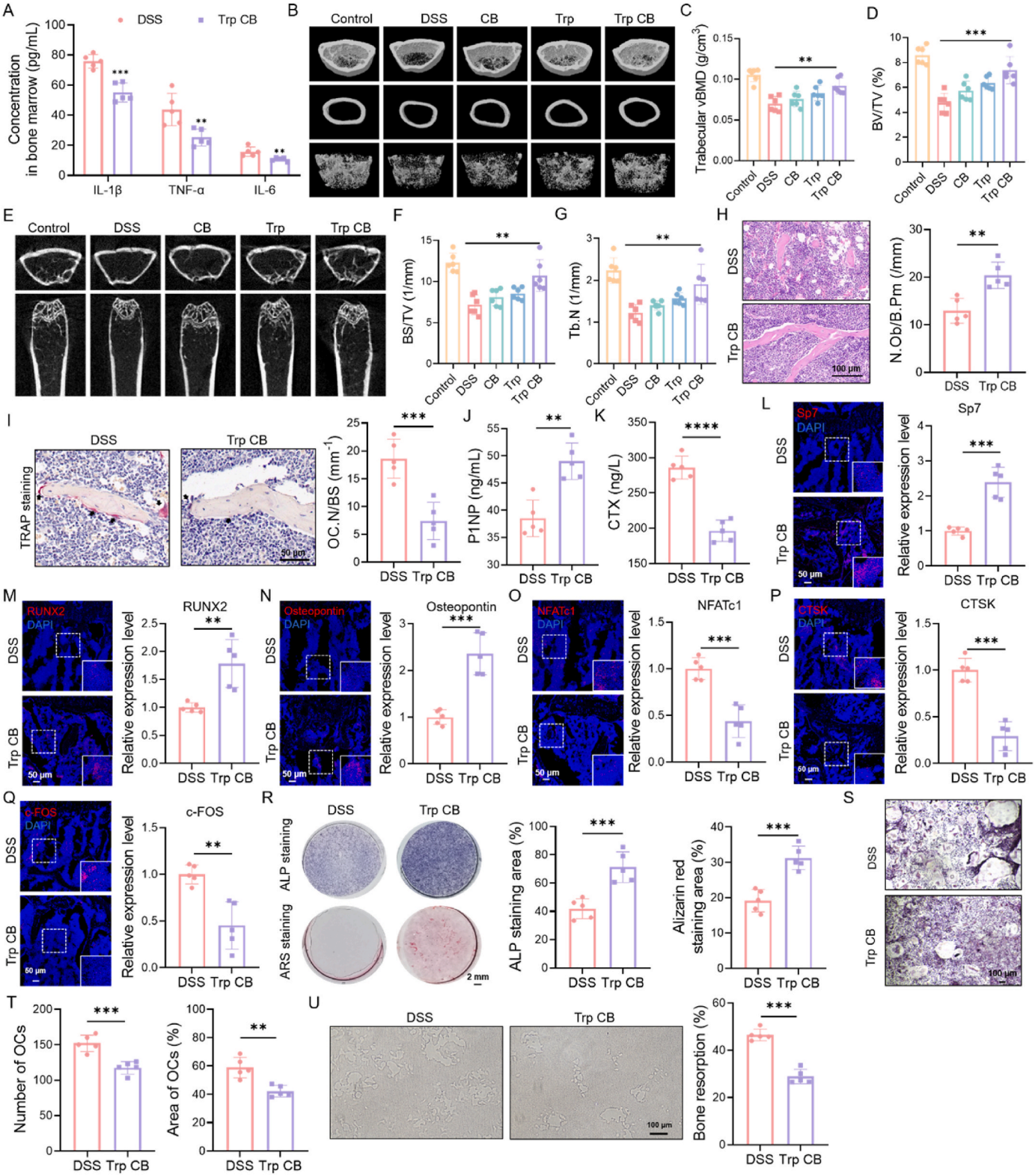

(caption on next page)

Fig. 4. Enhanced Bone Metabolism in Mice Treated with Engineered Tryptophan-producing probiotic. A. Levels of inflammatory cytokines in bone marrow from mice treated with tryptophan-producing probiotic compared to untreated controls, illustrating the anti-inflammatory effects of the probiotic. **B.** Three-dimensional μCT reconstructions of femurs from both groups, showing structural differences in bone. **C.** Quantitative analysis of bone density from the μCT data depicted in Panel B (n = 6). **D.** Bone Volume to Total Volume ratio (BV/TV), demonstrating changes in bone density induced by tryptophan-producing probiotic treatment (n = 6). **E.** Representative μCT images of mouse femurs, providing a detailed view of bone architecture. **F.** Bone Surface to Total Volume ratio (BS/TV), assessing the surface characteristics of the bone (n = 6). **G.** Trabecular Number (Tb.N), a measure of bone structure and quality (n = 6). **H.** Representative H&E stained sections of femoral bone tissue, with quantitative analysis. Scale bar: 100 μm. **I.** Representative staining of femoral bone sections for TRAP with quantitative analysis of osteoclast activity. Scale bar: 50 μm. **J.** Serum levels of P1NP, indicating increased osteoblast activity in tryptophan-producing probiotic treated mice. **K.** Serum levels of CTX, reflecting bone resorption levels. **L, M, N.** Immunofluorescence staining for osteoblast-specific proteins Sp7, RUNX2, and Osteopontin, respectively, showing enhanced expression in tryptophan-producing probiotic treated mice. Scale bar: 50 μm. **O, P, Q.** Immunofluorescence staining for osteoclast-specific proteins NFATc1, CTSK, and c-FOS, respectively, indicating altered osteoclast function with tryptophan-producing probiotic treatment. Scale bar: 50 μm. **R.** Representative images and quantitative analysis of ALP and ARS staining for osteogenesis in bone marrow-derived mesenchymal stem cells. Scale bar: 2 mm. **S** and **T.** TRAP staining for osteoclastogenesis in bone marrow-derived mononuclear macrophages, with quantification of activity. Scale bar: 100 μm. **U.** Bone resorption assay demonstrating pit formation and quantifying resorption activity, highlighting the effects of tryptophan-producing probiotic on osteoclasts. Scale bar: 100 μm. Data are presented as mean ± SD; statistical significance was calculated by the Student's t-tests or one-way ANOVA. $*p < 0.05$, $**p < 0.01$, $***p < 0.001$, and $****p < 0.0001$. n = 5.

effectively alleviated by the treatment (Supplementary Figure 5J). The Wnt/β-catenin pathway involved in osteoblast differentiation and the NF-κB pathway related to osteoclast differentiation changed in response to the reduced inflammatory environment in the bone marrow (Supplementary Fig. 5K–L). Further assessments using μCT scans and reconstructions of mouse femurs revealed notable improvements in bone mass and architectural parameters following tryptophan-producing probiotic treatment (Fig. 4B–G). Histological evaluations corroborated these imaging findings. H&E staining demonstrated enhancements in bone microarchitecture (Fig. 4H), while TRAP staining showed a reduction in the number of osteoclasts in mice receiving tryptophan-producing probiotics (Fig. 4I), suggesting an inhibition of bone resorption processes. Serum bone turnover markers further supported these observations, with an increase in P1NP and a significant decrease in CTX, indicating stimulated bone formation and reduced bone degradation, respectively (Fig. 4J–K).

To understand the cellular mechanisms involved, we examined the expression of specific proteins associated with osteoblasts and osteoclasts *in vivo*. Immunofluorescence staining of bone tissue sections of mice treated with tryptophan-producing probiotics exhibited increased expression of osteoblast-specific proteins Sp7, RUNX2, and Osteopontin, which are essential for bone formation (Fig. 4L–N). In contrast, the expression of osteoclast-specific proteins NFATc1, CTSK, and c-FOS was downregulated (Fig. 4O–Q), indicating a suppression of osteoclast differentiation and activity. To investigate whether tryptophan secreted by the engineered bacteria has a direct impact on bone remodeling, we measured tryptophan levels in serum and bone marrow. While there was a significant change in serum tryptophan, no significant change was observed in bone marrow (Supplementary Fig. 5M–N), thus excluding a direct effect on bone remodeling. *In vitro* experiments further validated these findings. BMSCs from tryptophan-producing probiotic-treated mice showed enhanced osteogenic differentiation and mineralization (Fig. 4R). In addition, bone marrow-derived monocyte/macrophage precursors exhibited inhibited osteoclast differentiation and reduced bone resorption capabilities (Fig. 4S–U).

These comprehensive *in vivo* and *in vitro* analyses demonstrated that supplementation of tryptophan in colitis mice effectively modulates bone metabolism, enhancing bone formation while inhibiting resorption. This indicated that tryptophan-producing probiotics could be a promising therapeutic strategy for diseases characterized by excessive bone loss in patients with colitis.

2.5. Tryptophan-producing probiotic improves bone mass in elderly mice

The deterioration of intestinal barrier function was a common issue in aging, which correlated with the increased incidence of osteoporosis in elderly populations [34–36]. Aged mice demonstrated low-grade chronic inflammation compared to young mice (Supplementary Fig. 6A). To evaluate whether tryptophan-producing probiotics could mitigate this age-related osteoporosis, aged mice were orally treated with tryptophan-producing probiotics (Fig. 5A). Two weeks later, the mice were euthanized for analysis. Histological analysis revealed significant improvements in the intestinal tissue structure of the treated elderly mice compared with the control mice (Supplementary Figure 6B). Additionally, immunohistochemical analysis showed increased expression of the tight junction proteins ZO-1 and occludin (Fig. 5B–C) in treated mice, indicating a restoration of barrier integrity. Moreover, reductions in MPO activity and apoptosis in intestinal epithelial cells were observed (Supplementary Fig. 6C–D), further supporting the enhancement of barrier function.

The Wnt/β-catenin and NF-κB pathway changed following treatment in the bone marrow (Supplementary Fig. 6E–F). Additionally, TRAP staining of bone tissue further confirmed a reduction in the number of osteoclasts (Supplementary Fig. 6G). More importantly, parallel assessments of bone health were conducted using μCT scans and reconstructions of the femurs from the aged mice. In mice receiving tryptophan-producing probiotics, there was a notable improvement in both bone mass and structural parameters (Fig. 5D–J) without any significant side effects on other major tissues (Supplementary Figure 6H), highlighting the tryptophan efficacy in reversing bone loss associated with aging.

Overall, these results indicated that tryptophan-producing probiotic holds potential therapeutic effects for treating osteoporosis in the elderly by restoring intestinal barrier integrity and enhancing bone density. This action underscored the importance of gut health in maintaining skeletal integrity, particularly in the context of aging, and positions tryptophan as a promising candidate for treating senile osteoporosis.

3. Discussion

The composition of the gut microbiota plays a significant role in maintaining the integrity of the gut barrier, preventing the leakage of harmful substances such as bacteria, toxins, and undigested food particles into the bloodstream. However, inflammation within the gut, a common pathological feature in conditions like inflammatory bowel disease (IBD) and aging, can disrupt the gut epithelial barrier [34,37,38]. This can trigger inflammation and immune responses throughout the body, contributing to various diseases and conditions. For example, damage to the intestinal epithelial barrier leads to an increase in pathogen-associated molecular patterns (PAMPs) entering the liver via the portal vein, resulting in hepatic inflammation and promoting the progression of liver diseases [39]. Recent studies in patients with primary osteoporosis have documented changes in the composition and abundance of the gut microbiota [13,40]. Furthermore, experimental animal studies have demonstrated that inflammatory bone loss in osteoporotic models is attributable to the activation of gut-mediated immune responses [41,42]. Current research is also exploring the potential

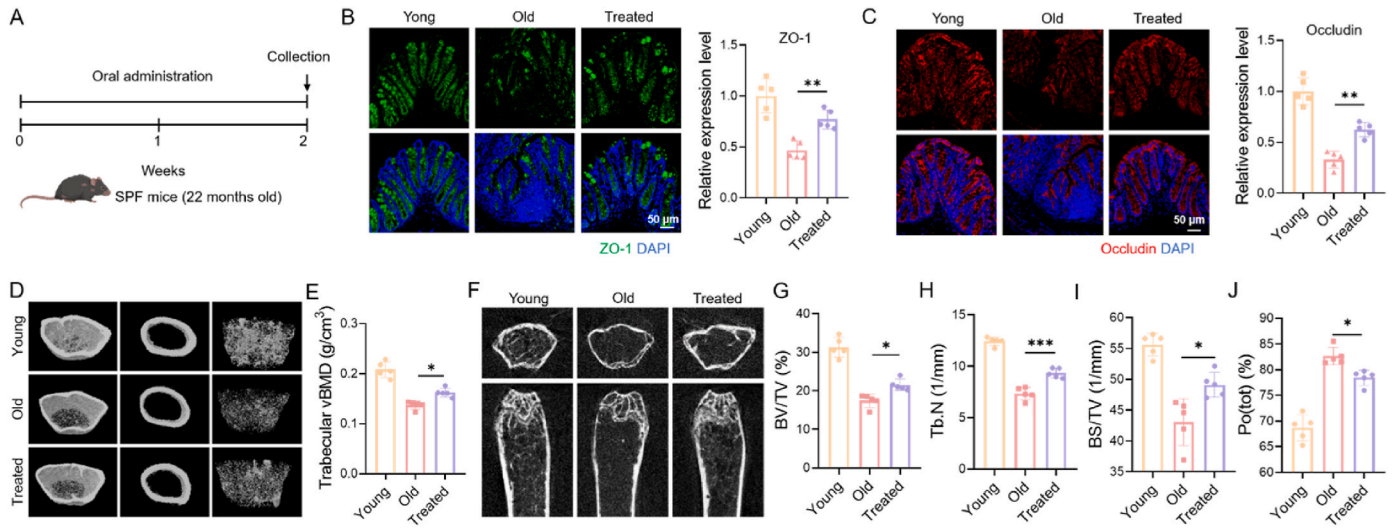

Fig. 5. Improvement of Intestinal Barrier Integrity and Bone Mass in Elderly Mice by Engineered *Clostridium butyricum*. **A.** Schematic representation of the treatment regimen with tryptophan-producing probiotic in elderly mice. **B** and **C.** Representative immunofluorescence images showing expression of the tight junction proteins ZO-1 and occludin in the intestines of elderly mice treated with tryptophan-producing probiotic compared to the untreated group. Scale bar: 50 μm. **D.** Three-dimensional μCT reconstructions of femurs from treated and controlled elderly mice, displaying bone structure. **E.** Quantitative analysis of bone density derived from the μCT scans shown in Panel D. **F.** Representative μCT scan images of mouse femurs, providing detailed views of bone quality and structure. **G.** Measurement of Bone Volume to Total Volume ratio (BV/TV), reflecting bone density improvements in treated mice. **H.** Measurement of Bone Surface to Total Volume ratio (BS/TV), which assesses the surface area of bones relative to their volume. **I.** Measurement of Trabecular Number (Tb.N), indicating the number of trabeculae per unit area, a crucial structural parameter of bone quality. **J.** Measurement of Total Porosity (percent) (Po(tot)), evaluating the porosity of the bone, which is significant for assessing overall bone health and strength. Data are presented as mean ± SD; statistical significance was calculated by one-way ANOVA. $*p < 0.05$, $**p < 0.01$, $***p < 0.001$, and $****p < 0.0001$. n = 5.

of probiotics to regulate gut homeostasis as a therapeutic approach for osteoporosis [43].

In this study, we observed significant bone loss in mice models of colitis, highlighting a pathological link between intestinal inflammation and bone health. The disruption of the intestinal barrier, induced by microbial dysbiosis and metabolic byproducts, downregulated the expression of tight junction proteins such as ZO-1 and occludin, impairing the integrity of adherens junctions. This barrier impairment escalated immune responses, elevating inflammatory levels in both circulatory and bone marrow tissues, which in turn compromised osteoblast differentiation and enhanced osteoclast activation, leading to bone resorption and overall loss.

Further microbial and metabolite analysis revealed decreased levels of amino acid metabolites, notably those involved in tryptophan metabolism. Tryptophan metabolism in the gut involves its direct conversion by the gut microbiota into bioactive molecules such as indole and its derivatives. Indole, indole-3-acetic acid, indole-3-propionic acid, indole-aldehyde, and indole-acrylic acid are all ligands for the aryl hydrocarbon receptor (AhR). AhR signaling is considered a key component of the barrier immune response and is crucial for maintaining gut homeostasis. AhR is a ligand-activated transcription factor that is widely expressed in intestinal epithelial and immune cells. Upon ligand binding, AhR induces the upregulation of tight junction proteins, mucins, and anti-inflammatory cytokines in epithelial cells, while downregulating pro-inflammatory cytokines [24,44,45]. In immune cells, AhR forms a heterodimer with the AhR nuclear translocator (Arnt), which then translocates to the nucleus and activates immune-regulatory genes, downregulating intestinal inflammatory cytokines and upregulating IL-22 expression [46]. This process helps to alleviate intestinal inflammation and maintain mucosal immune balance. Additionally, other tryptophan metabolites, such as kynurenic acid, exert mucosal protective and immune-regulatory effects by interacting with G-protein-coupled receptors expressed primarily on epithelial and immune cells [23]. By engineering the beneficial bacterium *Clostridium butyricum* to overexpress tryptophan, we were able to restore tryptophan metabolites. Treatment with this tryptophan-producing probiotic not only improved the integrity of the intestinal epithelial barrier but also reduced systemic and marrow inflammation, promoted osteoblast differentiation, and inhibited excessive osteoclast activation, thereby ameliorating bone remodeling and increasing bone mass.

Additionally, in aged mice, tryptophan-producing probiotic treatment improved age-related intestinal barrier dysfunction and increased bone mass, suggesting a potential therapeutic approach for age-associated osteoporosis, a prevalent condition linked to chronic inflammation. With advancing age, factors such as dietary changes, antibiotic usage, alcohol consumption, circadian rhythm disruptions, and psychological stress can affect protein homeostasis, leading to the loss of intestinal barrier integrity [20,47–49]. Disruption of the intestinal barrier is a common pathophysiological change in the elderly, and chronic impairment of this barrier can allow harmful substances to permeate the intestinal mucosa and enter the systemic circulation, thereby eliciting a systemic inflammatory response. As observed in our treatment group, recent studies have found that aging animals exhibit marked changes in tryptophan metabolism. Supplementation with microbial metabolites such as indole derivatives and kynurenine has been shown to protect against intestinal atrophy, maintaining gut barrier integrity [50]. Research on centenarian populations also suggests that tryptophan microbial metabolites play a crucial role in promoting gut health and longevity [51]. Similar to recent findings related to COVID-19-induced pathological bone loss [33], our study underscored the critical role of gut microbial metabolites and inflammatory responses in inflammatory bone loss (Fig. 6). Wnt/β-catenin and NF-κB are key pathways for osteoblast and osteoclast differentiation [52,53]. In this study, we found that interference by inflammatory mediators alters these differentiation processes, thereby affecting bone mass. The improvement of age-related intestinal barrier dysfunctions is increasingly recognized as pivotal to overall health [34,38,54,55], offering a potential therapeutic strategy against chronic diseases such as osteoporosis that accompany aging. New strategies for enhancing bone health treatment are proposed [56,57].

Considering that osteoporosis typically correlates with chronic inflammation [58–60], whether other types of osteoporosis could also

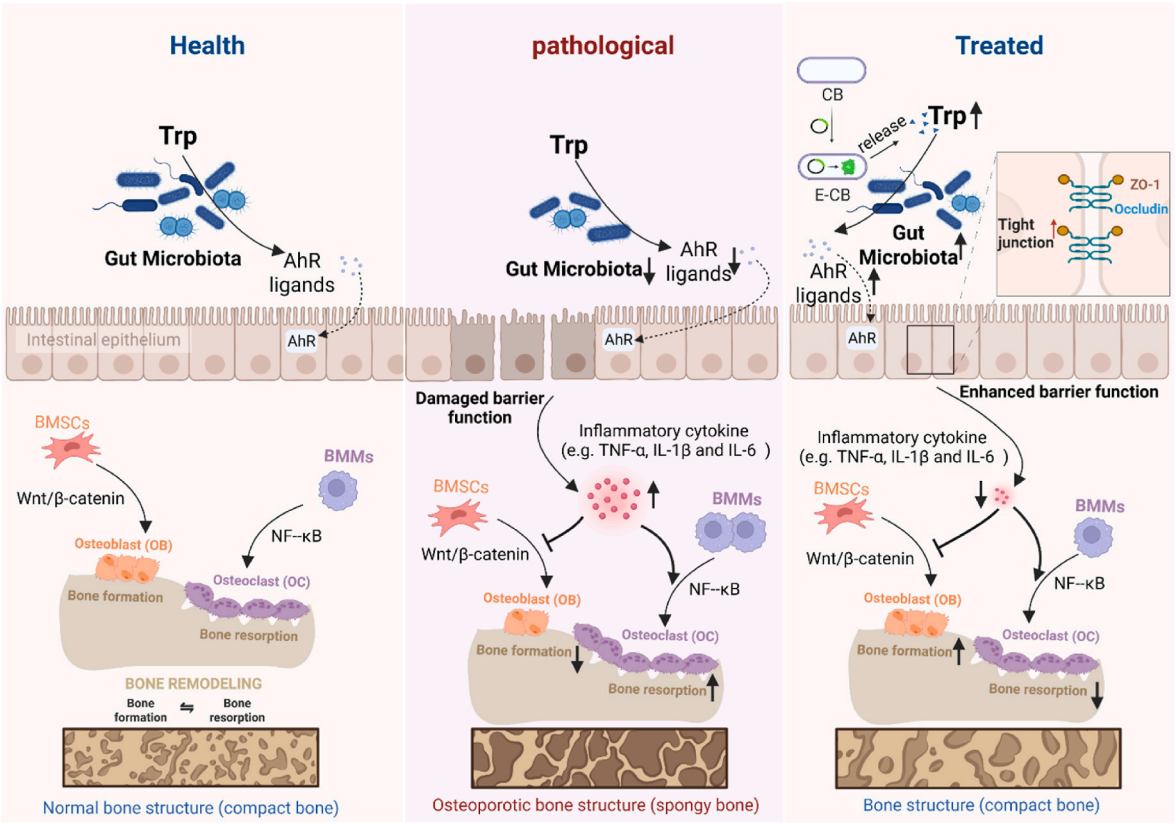

Fig. 6. Schematic representation of therapeutic action through the gut-bone axis mediated by Engineered *Clostridium butyricum*. Tryptophan-producing probiotics have been genetically customized to concurrently generate tryptophan-derived metabolites. The augmented production of these metabolites facilitates the restoration of compromised intestinal epithelial barriers, attenuates inflammatory responses, and promotes bone remodeling, ultimately leading to enhanced bone mass. Trp: Tryptophan. CB: *Clostridium butyricum*. Trp CB: Tryptophan-producing probiotic.

benefit from treatment with this engineered probiotic remains an area for future research. This opens new avenues for exploring microbial-based interventions as potential treatments for a range of inflammatory and age-related conditions.

4. Methods

Animal model. The animal studies were approved and performed following the guidelines of the Ethics Committee of our University (protocol number SUDA20231215A03). Female C57BL/6J mice, aged 8–12 weeks, were acquired from the Laboratory Animal Center at our University. Throughout the study, the animals were accommodated in ventilated cages located within a specific pathogen-free environment. The facility maintained a constant temperature of 22–24 °C and adhered to a 12-h light/dark cycle. Mice had unrestricted access to water and were fed Envigo Teklad global irradiated 18 % protein rodent diet meal 2918 as a standard diet. For the induction of chronic colitis, mice were given 1.5 % dextran sulfate sodium (DSS) in their drinking water ad libitum for 12 weeks, following the manufacturer's protocol for chronic inflammation models. In contrast, to model acute colitis, mice received drinking water containing 5 % DSS freely for one week, as per the established guidelines for acute inflammation models. For aging studies, elder mice models were utilized, selecting individuals aged 22 months.

μCT analysis. Micro-computed tomography (μCT) was conducted using a SkyScan 1174 system (SkyScan, Aartselaar, Belgium). The scans were performed under uniform parameters: voxel size was set at 10.3 μm, X-ray voltage at 50 kV, electric current at 810 μA, and rotation step at 0.5°. Three-dimensional (3D) reconstructions of the distal femur were carried out using CTvol software provided by the manufacturer. For the quantitative analysis of bone architecture, various static parameters were assessed. These parameters included bone mineral density (BMD), bone volume relative to tissue volume (BV/TV %), Total porosity (percent) (Po(tot)), bone surface relative to tissue volume (BS/TV), and trabecular number (Tb.N) for each analyzed sample. The quantification of bone parameters was conducted according to the 2013 ASBMR guidelines. For example, BS/TV was calculated by converting two-dimensional perimeter-to-area ratios (B.Pm/T.Ar) to three-dimensional surface-to-volume ratios using the 4/π correction factor (or 1.2 for iliac cancellous bone), with tissue volume (TV) as the referent.

Histological analysis. For histological examinations, mouse intestinal and femoral bone tissues were prepared as follows: Intestinal tissues were fixed and sectioned for Hematoxylin and Eosin (H&E) staining, and immunofluorescent labeling of tight junction proteins ZO-1 and occludin, as well as myeloperoxidase (MPO) and TUNEL assay to detect apoptosis. Femoral bones were first decalcified and then sectioned for further analysis. For bone tissue evaluation, 5-μm-thick sections were stained with H&E to assess the trabecular structure, and Tartrate-Resistant Acid Phosphatase (TRAP) staining was used to identify osteoclasts. Quantification of bone histological parameters was performed using OsteoMeasure software (OsteoMetrics Inc., Decatur, GA, USA). To analyze bone-related protein expression via immunofluorescence, 8-μm-thick longitudinally oriented sections of bone were stained with antibodies against osteoblast-specific proteins such as Sp7 (Abcam; ab209484), RUNX2 (Abcam; ab236639), and Osteopontin (Abcam; ab283656). Additionally, osteoclast-specific proteins NFATc1 (Santa; sc-7294), CTSK (Abcam; ab187647), and c-FOS (Abcam; ab222699) were also targeted. Immunofluorescent images were captured using an LSM 800 confocal microscope (Zeiss, Germany). The relative expression levels of these proteins were quantified using ImageJ software.

Calcein Labeling Experiment. For the calcein labeling experiment, tibial samples were obtained from mice that underwent a dual injection protocol of calcein. The first injection of 15 mg/kg calcein was administered 10 days before euthanasia, followed by a second injection of the same dose (15 mg/kg) 3 days before euthanasia. Following euthanasia, the tibias were carefully extracted and processed into hard tissue sections. These sections were then examined under a fluorescence microscope to capture images of the calcein incorporation. For the mineral apposition rate (MAR), the protocol involved measuring the inter-label distance at the midpoint of the double calcein labels, which was then standardized to the time interval between the labeling periods.

ELISA assay. Blood samples from the mice were collected and allowed to clot at room temperature for 30 min. Subsequently, these samples were centrifuged at 3500×*g* for 10 min. The serum obtained was aliquoted and stored at −80 °C until analysis. Enzyme-linked immunosorbent assay (ELISA) was utilized for the quantification of specific serum markers. The levels of RANKL and OPG in the mouse serum were measured using ELISA kits according to the protocols provided by R&D Systems. Additionally, the serum concentrations of the bone turnover markers P1NP and CTX were determined using ELISA kits from Nanjing Jiancheng Bioengineering Institute. For cytokine profiling, serum levels of IL-1β, TNF-α, and IL-6 were quantified using specific ELISA kits supplied by Invitrogen, USA, following the manufacturer's detailed instructions.

***In Vitro* Cell Experiments.** Mesenchymal stem cells (MSCs) and bone marrow macrophages (BMMs) were isolated from the long bones of C57BL/6 mice after 12 weeks of DSS-induced chronic colitis. The bone marrow-derived mesenchymal stem cells (BMSCs) were harvested and cultured as detailed in our previous studies [28,61]. BMSCs were plated in 12-well plates and cultured in an osteogenic medium composed of complete DMEM supplemented with 10 mM β-glycerophosphate, 50 μg/mL ascorbic acid, and 10 nM dexamethasone. For alkaline phosphatase (ALP) activity assessment, cells were stained using a BCIP/NBT Alkaline Phosphatase Color Development Kit (Beyotime Biotech, Shanghai, China) after 14 days of osteogenic induction. Additionally, for calcium deposition analysis, Alizarin Red S staining was performed using a Calcium Stain Kit (Modified Alizarin Red S Method) (Solarbio, Beijing, China) following 21 days of differentiation.

For osteoclast formation, bone marrow cells were extracted by flushing femurs and tibias with α-MEM. These cells were initially cultured in full α-MEM (containing 10 % FBS and 1 % penicillin-streptomycin) at 37 °C and 5 % CO_2 overnight to allow attachment. Nonadherent cells were then cultured in α-MEM supplemented with 30 ng/mL M-CSF (R&D Systems) for 3 days to derive BMMs. BMMs were seeded at a density of 1×10^4 cells/well in 96-well plates in medium enriched with 30 ng/mL M-CSF and 50 ng/mL RANKL (R&D Systems) and cultured for 5–7 days. Osteoclasts were fixed with 4 % paraformaldehyde, stained for tartrate-resistant acid phosphatase (TRAP) using an acid phosphatase leukocyte kit (Sigma-Aldrich, Darmstadt, Germany), and identified as TRAP-positive multinucleated cells with three or more nuclei under an Olympus microscope (Waltham, MA, USA). For the bone resorption assay, BMMs were cultured on hydroxyapatite-coated 24-well plates (Corning Inc., Corning, NY, USA) in full medium supplemented with M-CSF and RANKL. The medium was refreshed every two days. After 5 days, cells were cleaned with 5 % sodium hypochlorite, and resorption pits were imaged. The area of bone resorption was quantified using ImageJ software.

To simulate the proinflammatory microenvironment in bone marrow, the culture medium was supplemented with 1 ng/mL recombinant murine IL-1β (R&D Systems, USA).

Western blotting. Cells were washed with PBS and lysed on ice using RIPA buffer containing protease inhibitors. The lysates were then centrifuged at 12,000 g for 15 min to collect the supernatants, and protein concentrations were determined using the BCA Protein Assay Kit (Thermo Fisher, USA). Equal amounts of protein (20 μg) were separated by SDS-PAGE and transferred to PVDF membranes (Bio-Rad, Hercules, CA, USA). The membranes were blocked with 5 % nonfat milk and incubated overnight at 4 °C with primary antibodies. Following incubation, the membranes were washed and incubated with HRP-conjugated secondary antibodies. Protein bands were detected using chemiluminescent substrate (ECL). Band intensities were quantified with ImageJ software. The original Western blot data are shown in Supplementary Figure 7.

Real-time quantitative polymerase chain reaction (RT-qPCR) assay. Total RNA was isolated from the cells using TRIzol reagent (Biosharp, Hefei, China) according to the manufacturer's protocol. cDNA synthesis was performed using NovoScript®Plus All-in-one 1st Strand cDNA Synthesis SuperMix (gDNA Purge) (Novoprotein, Shanghai, China). Quantitative PCR was conducted using NovoStart® SYBR qPCR SuperMix Plus (Novoprotein, Shanghai, China) on a LightCycler480 Real-time PCR system (Roche, USA). The expression levels of target genes were normalized to GAPDH, and relative gene expression was calculated using the ΔΔCt method. The primer sequences used in the analysis are listed in Supplementary Table 1.

Flow cytometry analysis. To detect the changes in the immune microenvironment of the intestines and bone marrow after different treatments, we collected the intestines of mice and obtained single-cell suspensions of the intestines through tissue fragmentation. Then, cells were stained with APC-CD45, FITC-F4/80 and PE-CD3 antibodies to evaluate the number of macrophages and T cells. To analyze the activation status of macrophages in intestines, PE-CD80 and APC-CD206 were stained to observe the polarization of macrophages. PE-CD3, APC-CD8a, and FITC-CD4 were stained to evaluate the activation state of T cells. At the same time, PE-IFN-γ, APC-TNF-α, APC-IL-17A, and APC-IL-4 staining was applied to examine the activation state of $CD4^+$ T cells. The gating strategy for flow cytometry analysis of intestinal and bone marrow tissues is presented in Supplementary Figure 8.

16S rRNA gene sequencing assay. Post-treatment, fecal samples from the experimental animals were immediately collected, snap-frozen in liquid nitrogen, and shipped to GENEWIZ Company for gut microbiota profiling using 16S rRNA gene sequencing. DNA was extracted from these samples using a commercial DNA extraction kit, ensuring high-quality genetic material for subsequent analyses. The concentration of the extracted DNA was quantified using the Qubit® dsDNA HS Assay Kit. A second-generation sequencing library was then prepared, and the library concentration was determined using a Tecan Infinite® 200 Pro enzyme labeler. Following library quantification, paired-end sequencing (PE250/FE 300) was conducted on an Illumina MiSeq/Novaseq system (Illumina, San Diego, CA, USA), according to the manufacturer's guidelines to generate raw sequencing data. Data filtering was applied to obtain high-quality sequences for analysis.

The raw sequencing data underwent initial processing, where paired-end reads were merged, and sequences resulting from the assembly were subsequently filtered based on a minimum length criteria of 200 bp. Quality filtering was performed to remove low-quality and chimeric sequences. The high-quality sequences were then subjected to Operational Taxonomic Unit (OTU) clustering and sequence clustering using VSEARCH (version 1.9.6), with a sequence similarity threshold set at 97 %. Representative sequences from each OTU were taxonomically classified using appropriate databases. The microbial composition of each sample was quantified at various taxonomic levels, allowing for detailed analysis of the gut microbiota structure and diversity across different treatment groups.

SCFAs detection by gas chromatography-mass spectrometry quantitation. The detection of short-chain fatty acids was based on previous reports [62]. Fecal samples were collected immediately following defecation, promptly ground in liquid nitrogen, and stored at −80 °C until processed. For SCFA extraction, 100 mg of each fecal sample was homogenized with 1000 μL of ultrapure water. This mixture was then incubated at 4 °C for 30 min to facilitate extraction. Following incubation, the samples were centrifuged at 13,000×*g* for 30 min to obtain the supernatant. From the resulting supernatant, 100 μL was

transferred to a new 0.6 mL glass tube. To acidify the sample, 10 μL of 5 M HCl was added, adjusting the pH to approximately 2. Subsequently, 100 μL of anhydrous n-hexane (1:1, v/v) was added to the acidified homogenate. The mixture was incubated on ice for 5 min and centrifuged at 10,000×*g* for 5 min. The n-hexane layer containing SCFAs was carefully transferred to a new tube containing anhydrous Na_2SO_4 to desiccate any residual water. This extraction process was repeated twice with additional n-hexane to ensure thorough recovery of SCFAs.

For derivatization, 100 μL of the pooled n-hexane extracts were transferred to a glass GC vial insert. To this, 5 μL of BSTFA was added for silylation, and the vial was immediately capped and rotated to mix. The derivatization reaction was carried out by incubating the samples at 70 °C for 20–40 min, 37 °C for 2 h, or at room temperature (25 °C) overnight, exceeding 8 h. The derivatized samples were then analyzed using GC/MS. Blank sample was processed with the same procedure as that of fecal samples. The corrected peak area of acetic acid is calculated by those peak areas of samples minus that of the blank sample detected under the same conditions. The GC system was equipped with a helium carrier gas flowing at a rate of 1 mL/min. A total volume of 10 μL of the derivatized sample was injected with a solvent delay time set at 3 min and a split ratio of 10:1. The initial column temperature was set at 40 °C, held for 2 min, then ramped at 15 °C/min to 150 °C, held for 1 min, further ramped at 30 °C/min to 300 °C, and held for 5 min. Ionization was performed in electron impact (EI) mode at 70 eV. Mass spectra were collected from *m/z* 40 to 400 in full scan mode at a frequency of 12.8 scans per second. Compounds were identified by comparing the retention times and mass spectra with those of purified standards. Quantification was performed using target ions in selected ion monitoring (SIM) mode.

Untargeted metabolomics. Mouse fecal samples were preserved in liquid nitrogen immediately after collection and shipped to APTBIO (Shanghai, China) for analysis. Upon arrival, samples were gradually thawed at 4 °C. For extraction, an aliquot of each sample was added to a pre-chilled solvent mixture of methanol, acetonitrile, and water in a 2:2:1 vol ratio. The samples were then subjected to vortex mixing followed by low-temperature ultrasonication for 30 min. Subsequently, the mixtures were incubated at −20 °C for 10 min and centrifuged at 14,000 g at 4 °C for 20 min. The resulting supernatant was collected and vacuum-dried for further analysis. For mass spectrometry, the dried extracts were reconstituted in 100 μL of an acetonitrile-water solution (1:1, v/v). This mixture was then centrifuged at 14,000 g for 15 min at 4 °C to clarify the solution. The clear supernatant was transferred to a new tube and subjected to high-resolution accurate mass spectrometry.

The analysis was conducted using a Vanquish UHPLC (Thermo) coupled with an Orbitrap mass spectrometer at Shanghai Applied Protein Technology Co., Ltd. For hydrophilic interaction liquid chromatography (HILIC) separation, a 2.1 mm × 100 mm ACQUITY UPLC BEH Amide 1.7 μm column (Waters, Ireland) was employed. The mobile phase consisted of A = 25 mM ammonium acetate and 25 mM ammonium hydroxide in water, and B = acetonitrile, in both ESI positive and negative modes. The gradient began with 98 % B for 1.5 min, which was linearly reduced to 2 % over 10.5 min, maintained for 2 min, and then increased back to 98 % in 0.1 min, followed by a 3-min re-equilibration phase.

The ESI source parameters were set as follows: Ion Source Gas1 and Gas2 at 60, curtain gas (CUR) at 30, source temperature at 600 °C, and IonSpray Voltage Floating (ISVF) at ±5500 V. For MS-only acquisition, the instrument scanned over the *m/z* range of 80–1200 Da with a resolution of 60,000 and an accumulation time of 100 ms. In auto MS/MS acquisition, the range was 70–1200 Da with a resolution of 30,000 and an accumulation time of 50 ms, with an exclusion time of 4 s.

Raw MS data were converted to MzXML files using ProteoWizard MSConvert and imported into XCMS software for analysis. Peak picking was performed using the parameters: centWave *m/z* = 10 ppm, peakwidth = [10,60], prefilter = (10, 100). For peak grouping, the parameters were set as bw = 5, mzwid = 0.025, and minfrac = 0.5. Isotope and adduct annotations were performed using CAMERA (Collection of Algorithms for Metabolite Profile Annotation). Only extracted ion features with more than 50 % non-zero values in at least one group were retained. Compound identification was based on accurate *m/z* values (<10 ppm) and MS/MS spectra compared with an in-house database of authentic standards.

Following sum-normalization, the data were analyzed using the R package (ropls), and multivariate analyses were conducted, including Pareto-scaled principal component analysis (PCA) and orthogonal partial least-squares discriminant analysis (OPLS-DA). Model robustness was evaluated using 7-fold cross-validation and response permutation testing. The variable importance in projection (VIP) values from the OPLS-DA model were used to assess the contribution of each variable to classification. Student's t-test was applied to compare two independent sample groups, with VIP >1 and $p < 0.05$ used to identify significantly altered metabolites. Pearson's correlation analysis was performed to evaluate the relationship between variables.

Engineering tryptophan-producing probiotic. The designed recombinant plasmid image was shown in Supplementary Fig. 9A. The Clostridium-E. coli shuttle overexpression vector pMTL82151 was first used, and the strong promoter Pthl was cloned and inserted into the vector pMTL82151, which was constructed by first amplifying the primer using thl-XbaI-F/R. It was then used as a template for double digestion with pMTL82151 using primers for thl-F/R and digested with XbaIand XhoIrestriction endonucleases. The digested product was recovered and plasmid pMTL82151-thl was obtained. Gene synthesis was performed to obtain the structural gene sequences capable of expressing tryptophan biosynthetic enzymes (trpE, D, C, B, A) on the E. coli tryptophan manipulator, and then the desired structural gene fragments were amplified by polymerase chain reaction (PCR) using the primers and the appropriate restriction enzyme recognition sites on both sides. The pMTL82151-thl plasmid was then digested with the appropriate restriction endonuclease, and the digested products were recovered for ligation reaction. The amplified trpEDCBA gene fragment was inserted into the plasmid pMTL82151-thl to form the recombinant plasmid "pMTL82151-trpEDCBA". Recombinant plasmids were heat-stimulated and transformed into E. coli and single colonies were picked for the next step in chloramphenicol-containing LB medium. Clostridium butyricum (CB) was cultured in a liquid thioglycolate medium. Then, E. coli and Clostridium butyricum were mixed and coated on RCM plates for anaerobic incubation at 37 °C. The pMTL82151-trpEDCBA in E. coli was transferred to the Clostridium butyricum strain by conjugation. Subsequently, the bacteria on the plates were collected and spread onto RCM plates containing methicillin for antibiotic screening culture. Single colonies were singled out for further culture in a liquid thioglycolate medium to obtain the mutant strain tryptophan-producing probiotic. Besides, the full-length plasmid sequencing analysis was conducted and the results indicated that the sequence integrity of the plasmids was complete (Supplementary Fig. 9B).

Transmission electron microscopy (TEM, FEI TF20) and Zetasizer Nano ZS instruments (Nano ZS90, MALVERN) were used to observe the morphology of the bacteria and to characterize the particle size distribution and zeta potential of the tryptophan-producing probiotic. CB and tryptophan-producing probiotics were incubated statically at 37 °C in chloramphenicol (15 μg/ml) or chloramphenicol-free thioglycolate medium. The effect of the engineered tryptophan-producing probiotic on the growth state of the bacteria was analyzed by measuring the absorbance of the bacterial samples at 600 nm with a UV spectrophotometer at the indicated time points. To determine the production of tryptophan and butyrate by tryptophan-producing probiotic, the bacteria stored at −80 °C were incubated in anaerobic test tubes in thioglycolate medium supplemented with chloramphenicol (15 μg/ml) at 37 °C for 24 h. The bacterial cultures were then centrifuged at 12000 rpm for 10 min and the bacterial supernatants were prepared by filtration through a 0.2 μm filter. High-performance liquid chromatography

(HPLC; Thermo, UltiMate 3000) was used to determine tryptophan and butyrate in the bacterial supernatants. The HPLC detection conditions for tryptophan were as follows: tryptophan was detected from the supernatant by a linear program of 10 % methanol and 90 % 0.03 % KH2PO4 for 18 min. The solvent flow rate was 1.0 ml/min. The amount of tryptophan (mg/ml) was analyzed by comparing the peak height (λ_{max}278 nm) or peak area of the sample with that of the analytical standard (Yuanye, Shanghai, China). The HPLC detection conditions for butyrate were as follows: butyrate was detected in the supernatant in a linear program of 20 % acetonitrile and 80 % 0.1 % phosphoric acid for 9 min with a solvent flow rate of 0.8 ml/min. Peak heights (λ_{max}206 nm) or peak areas of the samples were compared with those of the analytical standards (Beyotime, Nanjing, China), and the concentrations of butyrate (mg/ml) were calculated.

***In vivo* mouse experiment with tryptophan-producing probiotic.** For chronic colitis mice (C57BL/6J) therapeutic experiments, the experimental mice were randomly divided into five groups. The colitis mice were gavaged with PBS for each mouse in the DSS group. The normal mice were used as positive controls. For the CB and tryptophan-producing probiotic group, the CB and tryptophan-producing probiotic strains were freshly cultured in thiolglycollate medium, then resuspended in sterile PBS each day and were treated gavaged with 5×10^8 CFU/d for each colitis mouse. The CB and Trp CB group were received a daily gavage treatment of 5×10^8 CFU of probiotic strains. The Trp group of mice were received by adding 40 g kg^{-1} to the standard 2 g kg^{-1} conventional diet. The experimental period for gavage tryptophan-producing probiotics was two weeks.

For the aged mice (22-month-old, C57BL/6J) therapeutic experiments, the gavage of tryptophan-producing probiotic bacteria was treated with the same experimental methods, dosage, and period of gavage as in the treatment of chronic colitis mice. The control group was given PBS for each mouse.

Tryptophan diet. Mice were given either a conventional diet (Envigo Teklad global irradiated 18 % protein rodent diet meal 2918) or a tryptophan (Trp)-supplemented diet ad libitum in feeding jars. The tryptophan diet was prepared by adding 40 g kg^{-1} to the standard 2 g kg^{-1} conventional diet.

Evaluation of Tryptophan levels in blood serum and bone marrow. For each group of mice, performed orbital blood collection, then placed it at 4 °C for 1 h to stand. After that, centrifuged the collected blood at 7000 revolutions per minute (r/min) for 15 min, and took the supernatant to obtain the blood serum. Regarding the preparation of mouse bone marrow, after euthanizing the mice by cervical dislocation, the muscle tissue was removed and the bones were cleaned. The ends of the femurs were cut off, and a syringe was used to draw up physiological saline. The two femurs were flushed repeatedly through one end, collecting the bone marrow cells into a centrifuge tube. The collected bone marrow cells were then centrifuged at 1000 revolutions per minute (r/min) for 10 min, and the supernatant was discarded to obtain the bone marrow. The blood serum samples and treated mouse bone marrow homogenates were added with 6 % perchloric acid. They were vortexed for 1 min, then allowed to stand for 5 min. After that, they were centrifuged at 10,000×*g* for 10 min, and the supernatant was taken for sample detection. The high-performance liquid chromatography was performed to detect the concentrations of tryptophan. The separation of tryptophan from supernatants was achieved with methanol containing Sodium acetate (15 mM, adjusted to pH 4.0 with glacial acetic acid) in a linear program started with 8 % acetonitrile and 92 % Sodium acetate in 9 min of isocratic programs. The solvent flow rate was 1.2 ml/min. Tryptophan (mg/ml) was analyzed by comparing the peak height (λ_{max}280 nm) and peak areas of the samples with analytical standards (Yuanye, Shanghai, China).

***In vivo* toxicity assessment.** Ten female C57BL/6J mice, aged 8–12 weeks, were allocated into two groups, with five mice per group. One group received oral gavage of phosphate-buffered saline (PBS) as a control, while the other was administered engineered *Clostridium butyricum* for two weeks to assess the biosafety of the treatment. Following the treatment period, major organs including the liver, kidneys, spleen, heart, and lungs were harvested from all mice. These organs were then fixed, sectioned, and stained with H&E for histopathological examination.

Statistical analysis. For all experiments, a minimum of three independent trials were conducted. Quantitative data obtained from these trials were expressed as the mean ± standard deviation (SD). Statistical analyses were performed using GraphPad Prism version 8 software (GraphPad Software, Inc., La Jolla, CA, USA). Depending on the data distribution and experimental design, either one-way analysis of variance (ANOVA) or Student's two-tailed t-tests were applied to assess the statistical significance between groups. In the graphical representations of the data, statistical significance was denoted as follows: $*p < 0.05$, $**p < 0.01$, $***p < 0.001$, and $****p < 0.0001$. Cases, where differences were not statistically significant, were indicated by "ns".

CRediT authorship contribution statement

Bo Tian: Writing – original draft, Investigation. **Heng Wang:** Investigation. **Yue Zhang:** Investigation. **Jinmin Lv:** Investigation. **Dongxiao Li:** Investigation. **Chenmeng Zhou:** Methodology. **Jialu Xu:** Methodology. **Yichao Ni:** Methodology. **Bingbing Wu:** Methodology. **Mingchao Zhang:** Methodology. **Huaxing Dai:** Investigation. **Fang Xu:** Methodology. **Jinyu Bai:** Validation, Supervision. **Chao Wang:** Writing – review & editing. **Xiaozhong Zhou:** Supervision, Methodology.

Ethics approval and consent to participate

The animal studies were approved and performed following the guidelines of the Ethics Committee of Soochow University (protocol number SUDA20231215A03).

Declaration of competing interest

The authors declare that they have no known competing financial interests or personal relationships that could have appeared to influence the work reported in this paper.

Acknowledgments

We gratefully acknowledge the National Natural Science Foundation of China for their grants (No. 32371476, 82172425, T2321005, 82102611, 82472515), Jiangsu Provincial Medical Key Discipline (Laboratory) project (JSDW202223), Gusu Health Talent Project (GSWS2021015, 2021(021)), Natural Science Foundation of Jiangsu Province (No. BK20210089) and the Postgraduate Research & Practice Innovation Program of Jiangsu Province (KYCX23_3271, KYCX22_3222). This work was partly supported by the Collaborative Innovation Center of Suzhou Nano Science & Technology, the Priority Academic Program Development of Jiangsu Higher Education Institutions (PAPD), and the 111 Project.

Appendix A. Supplementary data

Supplementary data to this article can be found online at https://doi.org/10.1016/j.bioactmat.2025.05.013.

References

[1] P.D. Cani, et al., Microbial regulation of organismal energy homeostasis, Nat. Metab. 1 (1) (2019) 34–46.
[2] J.J. Qin, et al., A human gut microbial gene catalogue established by metagenomic sequencing, Nature 464 (7285) (2010) 59–U70.
[3] Y. Belkaid, T.W. Hand, Role of the microbiota in immunity and inflammation, Cell 157 (1) (2014) 121–141.

[4] M.G. Rooks, W.S. Garrett, Gut microbiota, metabolites and host immunity, Nat. Rev. Immunol. 16 (6) (2016) 341–352.
[5] S.V. Lynch, O. Pedersen, The human intestinal microbiome in health and disease, New Engl J Med 375 (24) (2016) 2369–2379.
[6] V. Osadchiy, C.R. Martin, E.A. Mayer, The gut-brain Axis and the microbiome: mechanisms and clinical implications, Clin. Gastroenterol. Hepatol. 17 (2) (2019) 322–332.
[7] A. Albillos, A. de Gottardi, M. Rescigno, The gut-liver axis in liver disease: pathophysiological basis for therapy, J. Hepatol. 72 (3) (2020) 558–577.
[8] T.P. Wypych, L.C. Wickramasinghe, B.J. Marsland, The influence of the microbiome on respiratory health, Nat. Immunol. 20 (10) (2019) 1279–1290.
[9] I. Nemet, et al., A cardiovascular disease-linked gut microbial metabolite acts via adrenergic receptors, Cell 180 (5) (2020) 862–+.
[10] M.R. Mahmud, et al., Impact of gut microbiome on skin health: gut-skin axis observed through the lenses of therapeutics and skin diseases, Gut Microbes 14 (1) (2022).
[11] H. Tilg, A. Kaser, Gut microbiome, obesity, and metabolic dysfunction, J. Clin. Investig. 121 (6) (2011) 2126–2132.
[12] L.H. Quan, et al., Myristoleic acid produced by enterococci reduces obesity through brown adipose tissue activation, Gut 69 (7) (2020) 1239–1247.
[13] M. Das, et al., Gut microbiota alterations associated with reduced bone mineral density in older adults, Rheumatology 58 (12) (2019) 2295–2304.
[14] J.H. Wang, et al., Diversity analysis of gut microbiota in osteoporosis and osteopenia patients, PeerJ 5 (2017).
[15] S. Adam, et al., JAK inhibition increases bone mass in steady-state conditions and ameliorates pathological bone loss by stimulating osteoblast function, Sci. Transl. Med. 12 (530) (2020).
[16] J.J. Ni, et al., Assessing causal relationship from gut microbiota to heel bone mineral density, Bone 143 (2021).
[17] X. Lin, et al., Gut microbiota impacts bone via -valeric acid-related pathways, Nat. Commun. 14 (1) (2023).
[18] Y.W. Zhang, et al., Diets intervene osteoporosis via gut-bone axis, Gut Microbes 16 (1) (2024).
[19] K. Sjögren, et al., The gut microbiota regulates bone mass in mice, J. Bone Miner. Res. 27 (6) (2012) 1357–1367.
[20] J. Martel, et al., Gut barrier disruption and chronic disease, Trends Endocrin Met 33 (4) (2022) 247–265.
[21] E.L. Mitchell, et al., Reduced intestinal motility, mucosal barrier function, and inflammation in aged monkeys, J. Nutr. Health Aging 21 (4) (2017) 354–361.
[22] S.A. Scott, J.J. Fu, P.V. Chang, Dopamine receptor D2 confers colonization resistance via microbial metabolites, Nature 628 (8006) (2024) 180–185.
[23] A. Agus, J. Planchais, H. Sokol, Gut microbiota regulation of tryptophan metabolism in health and disease, Cell Host Microbe 23 (6) (2018) 716–724.
[24] S.A. Scott, J.J. Fu, P.V. Chang, Microbial tryptophan metabolites regulate gut barrier function via the aryl hydrocarbon receptor, P Natl Acad Sci USA 117 (32) (2020) 19376–19387.
[25] B. Lamas, et al., CARD9 impacts colitis by altering gut microbiota metabolism of tryptophan into aryl hydrocarbon receptor ligands, Nat. Med. 22 (6) (2016) 598. +.
[26] Y.L.S. Innocentin, et al., Exogenous stimuli maintain intraepithelial lymphocytes via aryl hydrocarbon receptor activation, Cell 147 (3) (2011) 629–640.
[27] A. Korecka, et al., Bidirectional communication between the Aryl hydrocarbon Receptor (AhR) and the microbiome tunes host metabolism, Npj Biofilms Microbi 2 (2016).
[28] F. Xu, et al., Mesenchymal stem cell-derived extracellular vesicles with high PD-L1 expression for autoimmune diseases treatment, Adv. Mater. 34 (1) (2022).
[29] S. Zhao, et al., An orally administered CeO @montmorillonite nanozyme targets inflammation for inflammatory bowel disease therapy, Adv. Funct. Mater. 30 (45) (2020).
[30] N.G. Kotla, et al., Inflammation-specific targeted carriers for local drug delivery to inflammatory bowel disease, Biomaterials 281 (2022).
[31] S. Adam, et al., JAK inhibition increases bone mass in steady-state conditions and ameliorates pathological bone loss by stimulating osteoblast function, Sci. Transl. Med. 12 (530) (2020).
[32] J.W. Guo, et al., Exosome-based bone-targeting drug delivery alleviates impaired osteoblastic bone formation and bone loss in inflammatory bowel diseases, Cell Rep. Med. 4 (1) (2023).
[33] W. Qiao, et al., SARS-CoV-2 infection induces inflammatory bone loss in golden Syrian hamsters, Nat. Commun. 13 (1) (2022).
[34] A.M. Salazar, R. Aparicio, R.I. Clark, M. Rera, D.W. Walker, Intestinal barrier dysfunction: an evolutionarily conserved hallmark of aging, Dis. Model. Mech. 16 (4) (2023).
[35] H. Liu, et al., Synthetic biology-based bacterial extracellular vesicles displaying BMP-2 and CXCR4 to ameliorate osteoporosis, J. Extracell. Vesicles 13 (4) (2024).
[36] J.W. Lewis, et al., Therapeutic avenues in bone repair: harnessing an anabolic osteopeptide, PEPITEM, to boost bone growth and prevent bone loss, Cell Rep. Med. 5 (5) (2024).
[37] J.R. Turner, Intestinal mucosal barrier function in health and disease, Nat. Rev. Immunol. 9 (11) (2009) 799–809.
[38] J. Zhang, et al., Age-associated decline in RAB-10 efficacy impairs intestinal barrier integrity, Nature Aging 3 (9) (2023) 1107. +.
[39] R. Wang, et al., Gut microbiome, liver immunology, and liver diseases, Cell. Mol. Immunol. 18 (1) (2021) 4–17.
[40] J.Q. He, et al., Gut microbiota and metabolite alterations associated with reduced bone mineral density or bone metabolic indexes in postmenopausal osteoporosis, Aging-Us 12 (9) (2020) 8583–8604.
[41] M.C. Yu, et al., Ovariectomy induces bone loss via microbial-dependent trafficking of intestinal TNF T cells and Th17 cells, J. Clin. Investig. 131 (4) (2021).
[42] M.C. Yu, et al., PTH induces bone loss via microbial-dependent expansion of intestinal TNF T cells and Th17 cells, Nat. Commun. 11 (1) (2020).
[43] M.Y. Guo, et al., GG ameliorates osteoporosis in ovariectomized rats by regulating the Th17/Treg balance and gut microbiota structure, Gut Microbes 15 (1) (2023).
[44] T. Bansal, R.C. Alaniz, T.K. Wood, A. Jayaraman, The bacterial signal indole increases epithelial-cell tight-junction resistance and attenuates indicators of inflammation, P Natl Acad Sci USA 107 (1) (2010) 228–233.
[45] M.F. Li, et al., Gut microbiota metabolite indole-3-acetic acid maintains intestinal epithelial homeostasis through mucin sulfation, Gut Microbes 16 (1) (2024).
[46] J.S. Lee, et al., AHR drives the development of gut ILC22 cells and postnatal lymphoid tissues via pathways dependent on and independent of Notch, Nat. Immunol. 13 (2) (2012) 144–U158.
[47] B.E. Barrios, et al., Brief disruption of circadian rhythms alters intestinal barrier integrity and modulates DSS-induced colitis severity in mice, Inflammation (2024), https://doi.org/10.1007/s10753-024-02162-8.
[48] C.H. Kuo, L.L. Wu, H.P. Chen, J. Yu, C.Y. Wu, Direct effects of alcohol on gut-epithelial barrier: unraveling the disruption of physical and chemical barrier of the gut-epithelial barrier that compromises the host-microbiota interface upon alcohol exposure, J. Gastroenterol. Hepatol. 39 (7) (2024) 1247–1255.
[49] R.H. McMahan, et al., Changes in gut microbiome correlate with intestinal barrier dysfunction and inflammation following a 3-day ethanol exposure in aged mice, Alcohol 107 (2023) 136–143.
[50] X.Y. Wang, et al., Age-, sex- and proximal-distal-resolved multi-omics identifies regulators of intestinal aging in non-human primates, Nature Aging 4 (3) (2024).
[51] T. Wilmanski, et al., Gut microbiome pattern reflects healthy ageing and predicts survival in humans, Nat. Metab. 3 (2) (2021) 274. +.
[52] S.Y. Zhu, W. Chen, A. Masson, Y.P. Li, Cell signaling and transcriptional regulation of osteoblast lineage commitment, differentiation, bone formation, and homeostasis, Cell Discov 10 (1) (2024).
[53] W.L. Yang, et al., TAZ inhibits osteoclastogenesis by attenuating TAK1/NF-κB signaling, Bone Res 9 (1) (2021).
[54] A.L. Man, N. Gicheva, C. Nicoletti, The impact of ageing on the intestinal epithelial barrier and immune system, Cell. Immunol. 289 (1–2) (2014) 112–118.
[55] M.C.C. Machado, F.P. da Silva, Intestinal barrier dysfunction in human pathology and aging, Curr. Pharm. Des. 22 (30) (2016) 4645–4650.
[56] H. Liu, J.T. Triffitt, Z. Xia, J. Su, Artificial intelligence-enabled studies on organoid and organoid extracellular vesicles 5 (2) (2024).
[57] J. Huang, et al., Future perspectives: advances in bone/cartilage organoid technology and clinical potential 5 (4) (2024).
[58] A. Cline-Smith, et al., Ovariectomy activates chronic low-grade inflammation mediated by memory T cells, which promotes osteoporosis in mice, J. Bone Miner. Res. 35 (6) (2020) 1174–1187.
[59] J.Y. Li, et al., Sex steroid deficiency-associated bone loss is microbiota dependent and prevented by probiotics, J. Clin. Investig. 126 (6) (2016) 2049–2063.
[60] R.H. Straub, M. Cutolo, R. Pacifici, Evolutionary medicine and bone loss in chronic inflammatory diseases-A theory of inflammation-related osteopenia, Semin. Arthritis Rheum. 45 (2) (2015) 220–228.
[61] H.J. Shan, et al., Gold nanorods modified by endogenous protein with light-irradiation enhance bone repair via multiple osteogenic signal pathways, Biomaterials 284 (2022).
[62] S.M. Zhang, H.B. Wang, M.J. Zhu, A sensitive GC/MS detection method for analyzing microbial metabolites short chain fatty acids in fecal and serum samples, Talanta 196 (2019) 249–254.